ELECTROMAGNETIC MELT PROCESSING: A PATHWAY TO NEW ADDITIVE MANUFACTURING TECHNOLOGIES FOR FUNCTIONAL HIGH-PERFORMANCE THERMOPLASTICS

Madara Mohoppu [a,b], Utsab Ayan [a,b], Oussama Oulhakem [b], Olivia McNair [c], Ahmed Al-Ostaz [b,d], Enrique Jackson [e], Byron S. Villacorta [a,f*]

[a] Department of Chemical Engineering, University of Mississippi, University, MS 38677, United States

[b] Center for Graphene Research and Innovation (CGRI), University of Mississippi, University, MS, 38677, United States

[c] School of Polymer Science and Engineering, University of Southern Mississippi, Hattiesburg, MS 39406, United States

[d] Department of Civil Engineering, University of Mississippi, University, MS 38677, United States

[e] Marshall Space Flight Center, National Aeronautics and Space Administration, Huntsville, AL 35808, United States

[f] School of Mechanical and Mining Engineering, University of Queensland, Saint Lucia, QLD 4067, Australia

*Corresponding author: E-mail: bsvillac@olemiss.edu

Keywords: Electromagnetic melt processing, High-performance thermoplastics, Nanocomposites, Electrical conductivity, Powder bed fusion

ABSTRACT

In this study, we apply the electromagnetic (EM) melt processing of thermoplastics on an innovative EM field-driven powder bed fusion additive manufacturing (AM) concept for high-performance functional parts: Selective Microwave Melting/Sintering (SMM/SMS). This technique leverages the EM susceptibility of carbon nanotube-coated polymer micro-pellets to achieve rapid, localized heating and powder fusion. Thus, selective microwave melting (SMM) was used to fabricate multilayer specimens made of recycled polyphenylene sulfide (rPPS) and carbon nanotubes (CNTs). The resulting SMM specimens exhibited very good interlayer integrity, localized fusion at pellet boundaries, and tolerable residual porosity, indicating effective fusion and acceptable consolidation. CNT-rich interphases were retained after irradiation, generating anisotropic electrically active network pathways and enabling conductivity enhancement at low filler content. At only 1.0 wt% CNT, the specimens exhibited electrical conductivity approximately three orders of magnitude higher than neat rPPS. Dynamic mechanical analysis showed improved viscoelastic response relative to neat rPPS, while tensile testing confirmed that the SMM-processed specimens retained practical mechanical integrity despite localized voids. These results demonstrate that SMM can effectively consolidate EM susceptible thermoplastic powder beds while preserving their segregated conductive networks. This may become a scalable route for producing multifunctional thermoplastic parts with low filler loadings, tunable anisotropy, and structured materials and parts. Overall, the findings suggest that EM field-based AM can help overcome key limitations of conventional thermoplastic processing by enabling scalable, energy-efficient fabrication of nanostructured composites and expanding AM to a broader range of resins, including high-performance thermoplastics with customized functional properties.

INTRODUCTION

Additive manufacturing (AM), commonly known as 3D printing, has become a cornerstone of the third industrial revolution by enabling layer-by-layer fabrication of complex structures with reduced material waste, shorter lead times, and unprecedented design freedom [1]. Since its introduction, AM has evolved from prototyping technology into an increasingly popular platform considered for end-use manufacturing in aerospace, biomedical, automotive, electronics, energy, and defense applications [2,3]. Despite this progress, the broad industrial adoption of AM remains constrained by several persistent limitations, including restricted material options, high processing cost, limited build speed, scalability challenges, anisotropy, and inconsistent part quality [4]. These limitations are especially pronounced when the target application demands a combination of structural performance, thermal resistance, and multifunctionality [5]. As a result, there is a continuing need for new and advanced material options and for developing innovative processing techniques and AM technologies that can extend the performance envelope of AM beyond its current boundaries.

In many AM technologies, polymeric feedstocks dominate because they are lightweight, inexpensive, readily processable, and compatible with a wide range of AM platforms. However, conventional polymer-based AM parts often lack the mechanical strength, thermal stability, chemical resistance, and functional properties required for demanding service conditions [6]. Even when metals or ceramics are used, AM parts may still suffer from surface roughness, residual porosity, dimensional inaccuracies, and limited mechanical reliability [7]. These shortcomings have motivated extensive research into potential composite feedstocks, hybrid processing and AM methods, and post-processing approaches designed to improve part performance [7]. Among these strategies, the use of nanocomposite resins, which involves advanced nanomaterials compounded into the polymer matrix, has emerged as particularly promising because it offers a means to simultaneously improve stiffness, strength, flow

behavior, interlayer adhesion, thermal stability, electrical conductivity, and other transport properties [8,9]. In this context, the 3D printing with multifunctional nanocomposites is especially attractive because it addresses not only the structural limitations of conventional AM polymers but also opens the way to parts made of advanced, robust, and functional materials.

Within this broader context, field-assisted processing has emerged as a potentially transformative route for next-generation AM. In this work, we highlight the use of electromagnetic fields to induce sintering or melting on electrically conductive thermoplastics, a method based on what we call "electromagnetic melt processing" [10,11]. Unlike conventional thermal processing approaches, which often rely on large thermal gradients to heat the entire build environment or on surface scanning with a low-power (10-100 W) laser or electron beam, the application of electromagnetic (EM) waves enables strong localized volumetric heating and selective energy deposition in the regions that are intrinsically susceptible to EM field absorption [10,12]. This is particularly attractive for susceptor materials that efficiently convert EM energy into heat, enabling rapid thermal activation without the need for bulk heating [13].

Selective microwave sintering (SMS) or microwave-assisted sintering (MAS) is an emerging powder bed fusion additive manufacturing concept that has found some application with ceramic and metal powders, but that remains at the research stage for thermoplastics [14,15]. Current studies focus on microwave heating behavior, process control, and the feasibility of selective powder-layer sintering or fusion [16,17]. The powder bed fusion family of AM processes has largely demonstrated the value of layer-wise fabrication from a spread powder bed [18]. However, most established powder bed systems rely on focused beam-based energy delivery, which can produce steep thermal gradients, and that depends strongly on the optical or absorptive properties of the irradiated surface [19]. In contrast, microwaves heat susceptible powder bed systems volumetrically, thereby reducing thermal gradients and

potentially enabling more efficient interparticle bonding, as well as interparticle and interlayer fusion. Nevertheless, microwave-based AM methods also remain highly material-dependent because EM coupling efficiency is influenced by particle size, packing density, bed architecture, and primarily by the intrinsic electrical and dielectric properties of the bed [20,21]. Another constraint is full control of the uniformity of deposition of microwave energy, especially on large parts. Interestingly, waveguides may help guide the EM energy deposition, and microwave lasers (i.e., MASER) may potentially be used to focus the EM beam on the powder bed to minimize such effects. This would yield the benefits of the volumetric effect of the EM field as well as those of laser-based AM technology, such as in selective laser sintering (SLS) [22,23].

A central point in the EM melt processing of thermoplastics is that most polymers are nearly transparent to microwave radiation (i.e., non-susceptible) and therefore absorb insufficient energy to heat effectively on their own when irradiated [24]. In contrast, carbon nanomaterials such as CNTs and graphene are effective susceptors, responsive to EM fields due to their electronic transport properties, morphologies, and their ability to form interconnected networks [25,26]. Under microwave irradiation, such networks can interact well with EM waves, leading to rapid and highly intense heating through a combination of dielectric loss, conductive loss, and interfacial polarization effects [27,28]. The resulting temperature rise can be extremely fast and localized, often occurring in regions where networks of nanoparticles form clusters of electrical dimensions large enough to interact with the waves [10]. Thus, when strategically arranged within or around polymer particles, these susceptible nanofillers can form conductive pathways that improve electrical transport throughout, reinforce the polymer skeleton, and enhance heat transfer [29]. Depending on loading level, dispersion and segregation state, and network architecture, graphitic carbon nanomaterials can form electrically percolated structures that dramatically alter how energy is absorbed and distributed within the composite material

[30]. This behavior creates a mechanism by which microwave energy can be converted into heat precisely where it is needed, triggering polymer softening, sintering, or even melting at interfacial and bulk regions [10]. In this sense, such network architectures can serve as controllably arranged susceptors that translate the EM input into thermal energy, thereby enabling the selective "activation" of the surrounding polymer regions next to the networks. Our team has studied this and reported it with different thermoplastics and carbon nanomaterials in previous works [10,31,32].

As previously mentioned, this selective heating mechanism based on EM susceptibility may be especially useful because it can promote higher local interparticle fusion and even interlayer bonding through interfacial remelting, reducing post-processing steps (e.g., annealing, smoothing) [31]. If properly controlled, such spatially localized heating can reduce thermal degradation, warpage, and energy consumption while still enabling sufficient thermal activation for fusion. EM melt processing is also particularly attractive for high-performance (HP) thermoplastics that have narrow processing windows or high melting temperatures, such as polyphenylene sulfide (PPS), polyether ether ketone (PEEK), and polyimide (PI) [33]. These HP materials offer excellent thermal and chemical resistance, but they are difficult to process using conventional AM methods because they require higher thermal input and tighter control over fusion conditions [34]. By localizing heating to microwave-responsive nanocarbon networks, it is in principle possible to rapidly sinter or even fully melt-fuse the HP polymer micro-pellets while preserving the overall integrity of the part [10]. This makes EM melt processing of thermoplastics an appealing route for expanding the range of polymer options that can be additively manufactured into structurally meaningful components and parts.

The present work thus applies the EM melt processing of EM-susceptible HP thermoplastics to enable potentially new AM technologies, such as Selective Microwave Sintering (SMS) or Selective Microwave Melting (SMM) powder bed fusion of thermoplastics. The central

hypothesis of this investigation is that strategically engineered CNT networks on the surface of HP thermoplastic micro-pellets can efficiently absorb microwave energy, generate rapid localized heating, and promote selective interfacial melting or sintering to produce parts made of functional HP nanocomposites. By leveraging the basic mechanisms of EM melt processing, the proposed approach seeks to expand the portfolio of materials options for AM to HP thermoplastics. Therefore, in this study, we use polyphenylene sulfide (PPS), a high-temperature resin, to produce additively manufactured 3-layer SMM specimens of simple but consistent geometry and dimensions. The microstructure, transport, and mechanical properties of the specimens are characterized. More broadly, this study proposes a foundational premise for future EM field-enabled additive manufacturing routes that integrate structural performance, thermal robustness, and functionality in a new materials platform for advanced HP applications (e.g., aerospace, space, military, energy, electronics, etc.).

EXPERIMENTAL

Materials

Recycled polyphenylene sulfide (rPPS) micro-pellets, obtained as post-industrial waste from Fortron® 0320-PPS supplied by Celanese Corporation (Irving, TX, USA), were used as the polymer matrix. This material exhibited a density of 1.35 $g \cdot cm^{-3}$, a melting point of 283 °C, and a glass transition temperature (T_g) of approximately 90 °C, as determined by differential scanning calorimetry (DSC). Prior to processing, the rPPS micropellets were dried at 120 °C under vacuum for 12 hours to eliminate residual moisture and to minimize thermo-oxidative and hydrolytic degradation during melt processing.

Commercial NC7000 multi-walled carbon nanotubes (CNTs), by Nanocyl S.A., Belgium, were employed as the susceptor nanomodifiers. NC7000 possesses a purity of > 90 %, a nominal average outer diameter of ~8 nm, a length of 10-30 μm, and a specific surface area of

approximately 240 $m^2.g^{-1}$. The CNTs were used as received without further modification or purification (i.e., pristine).

Powder Bed Formulation via Ball Milling

The CNTs and polymer micro-pellets were mixed via ball milling to achieve homogeneous dispersion and a uniform CNT coating on the micro-pellets, yielding an EM-susceptible powder bed. The mixing process was carried out using a vertical high-energy planetary ball mill (Model MSE PRO 4L, MSE Supplies) under dry conditions at a rotation speed of 200 rpm. Stainless steel balls of different diameters (twenty 5-mm, ten 10-mm, and two 20-mm) were used in each 500-mL stainless steel milling jar, which contained 20 g of the polymer-CNT mixed formulation at 1.0 wt% CNTs. A mixing time of 60 min was utilized to achieve thorough mechanical exfoliation of agglomerated CNTs, uniform coverage, and adhesion of CNTs to the polymer micro-pellet surfaces. As displayed in **Figure 1**, this procedure produced a thin layer of exfoliated and well-distributed but interconnected CNTs on the surface of the rPPS micro-pellets, which imparts electromagnetic susceptibility to the resultant "green" mixtures.

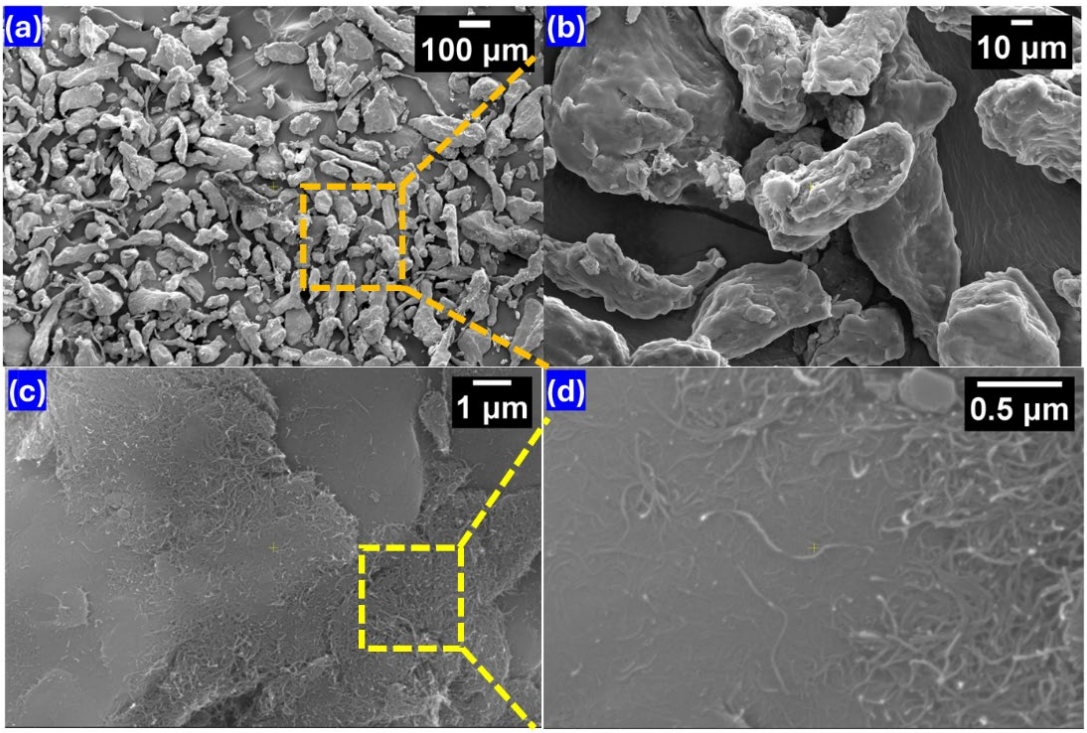

Figure 1. SEM micrographs showing the morphology of rPPS powder particles coated with 1 wt% CNTs at different magnifications: (a, b) low-magnification views of the powder particles, (c, d) higher-magnification images highlighting CNT coverage on the particle's surface.

Manufacturing of the SMM specimens

As depicted in **Figure 2**, using the EM-susceptible 1 wt% CNT/rPPS powder bed, we conducted proof-of-concept experiments for the selective microwave melting (SMM) powder bed fusion AM technique using a custom-fabricated glass mold. A total of five "rectangular" SMM specimens of ~60 mm in length, ~12 mm wide, and about 1.2 mm thick were prepared for this study. For each specimen, the first powder layer was uniformly spread into the mold (**Figure 2, step 1**). Then, it was subject to microwave irradiation using a custom-built laboratory microwave oven (Microwave Research & Applications, Inc. Model BP-095 UMISS). This oven delivers constant (non-cyclic) 2.45 GHz power. Irradiation was applied at 500 W for 30-60 seconds per layer (**Figure 2, step 2**), initiating localized heating, polymer melting, and fusion of the powder bed into a "monolithic" continuous SMM nanocomposite layer. Subsequent layers of the formulated powder were sequentially spread and leveled on top of the previously processed layer (**Figure 2c, step 3**), followed by repeated microwave exposure under identical

conditions. This layer-by-layer deposition and in-situ EM melt processing cycle was repeated until the desired part geometry was achieved (**Figure 2, step 4**). As depicted in **Figure 2,** most specimens required 3 layers to fill the cavity of the mold. Moreover, this method enabled the preparation of other types of simple geometries, as demonstrated by specimens of “T” and “L” shapes, which were also made to explore the shape versatility of the method (**Figure 2, step 4**).

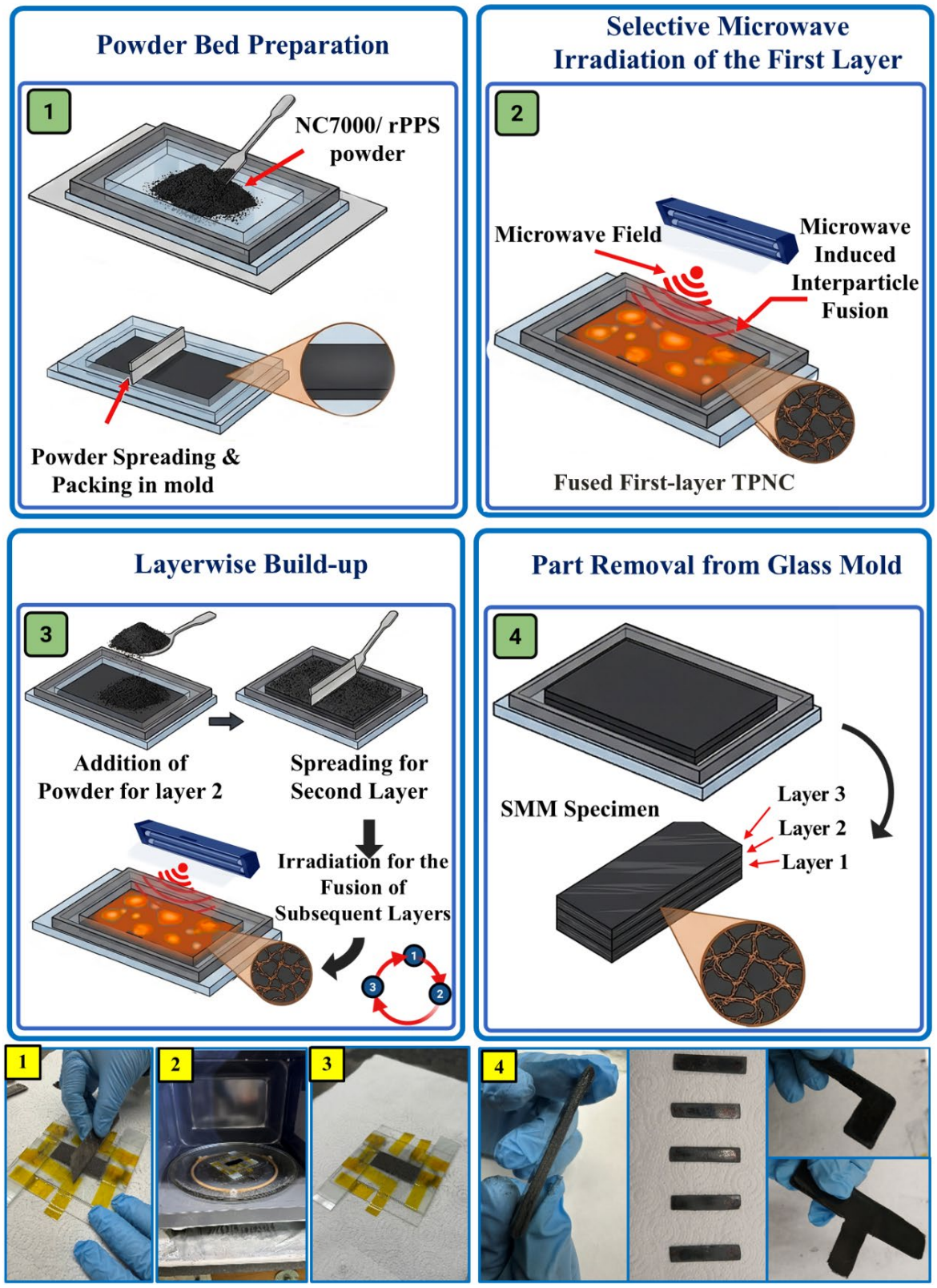

Figure 2. Schematic illustration of the SMM powder bed fusion AM process and photographic sequence of the fabrication of the three-layer SMM specimens: (1) powder bed preparation, (2) microwave irradiation of the first layer, (3) layer-wise build-up, and (4) removal of the SMM specimens from the mold, and specimens of different geometries.

Characterization

(1) Scanning Electron Microscopy (SEM)

The morphological and microstructural SEM analysis of the rPPS micro-pellets, CNTs, mixed powder bed, and SMM specimens was performed using a Thermo Fisher Quattro S Field-emission Environmental SEM at 15 kV in secondary electron mode. Prior to inspection, the materials and cryo-fractured specimens (for cross-section examination) were vacuum-dried to remove moisture and coated with a 5 nm gold layer using a LUXOR Au sputter coater.

(2) Volume Electrical Conductivity Measurements

The volume electrical conductivity, σ, of the SMM specimens was measured using a Keithley 6517B High-Resistance Electrometer with a custom-made guarded resistance test fixture, in compliance with ASTM D257. The fully shielded and grounded fixture enabled applied voltages ranging from 10 V to 500 V and provided current detection in the picoampere (pA) range. Measurements were performed using the alternating polarity method in the KickStart software to minimize charge-accumulation effects and reduce thermal-noise artifacts during testing. For each SMM specimen, in-plane and through-thickness conductivity measurements were taken; five measurements were conducted for each configuration, for which three consecutive readings were recorded and averaged to improve statistical reliability. The relative humidity during testing remained near 50% RH. The conductivity was calculated using Equation 1:

$$\sigma = \frac{l}{RA} \tag{1}$$

where l is the specimen "length" between the electrodes, R is measured resistance, and A is the electrode contact area.

(3) Dielectric characterization

The through-thickness dielectric properties of the SMM specimens were measured using an LCR meter (HIOKI IM3523) over the frequency range of 100 Hz to 200 kHz at room temperature. The measurements were performed using the parallel-plate capacitor method, in which each specimen was sandwiched between two flat electrodes to form a capacitor. Care was taken to ensure intimate contact between the sample surfaces and the electrodes using copper sticky foil so that air gaps were minimized during measurement. The analyzer provided the capacitance, C, and phase angle, θ, as a function of frequency.

The real part of the relative permittivity, $\varepsilon'/\varepsilon_0$, was then calculated from the measured capacitance using equation 4,

$$\varepsilon'/\varepsilon_0 = \frac{Cd}{A\varepsilon_0} \tag{4}$$

where C is the measured capacitance, d is the sample thickness, A is the electrode area, and ε_0 is the permittivity of free space. The imaginary part of the relative permittivity, $\varepsilon''/\varepsilon_0$, was calculated from the impedance phase angle, θ, response using equation 5:

$$\varepsilon''/\varepsilon_0 = -(\varepsilon'/\varepsilon_0)\left(\frac{1}{\tan\theta}\right) \tag{5}$$

(4) Mechanical Tensile Testing

Tensile testing was performed on the SMM specimens. The tests were conducted using a universal testing machine (Instron 68TM-10 series, Instron, USA) equipped with a 10 kN load cell. Testing was performed at a constant crosshead speed of 1 mm.min^{-1}, an initial gauge length of 30 mm, and data were acquired and collected using Blue Hill Universal software (Instron). All experiments were conducted under ambient laboratory conditions of approximately 25 °C and 50% relative humidity. The elastic modulus, ultimate tensile strength, and strain-at-break were determined from the resulting stress-strain curves.

(5) Dynamic mechanical analysis

Dynamic mechanical analysis (DMA) was performed to evaluate the viscoelastic response of the SMM specimens. The measurements were carried out using a Discovery DMA 850 Dynamic Mechanical Analyzer, using a temperature ramp from room temperature to 300 °C at a heating rate of 10 °C min^{-1}. Storage modulus (E'), loss modulus (E''), and damping factor (tan δ) were recorded as a function of temperature. The specimens were tested under constant oscillatory loading within the linear viscoelastic regime (i.e., 0.05% strain) at a frequency of 6.28 Hz, using a tension-mode geometry fixture. All measurements were performed on the neat rPPS and the SMM specimens to enable direct comparison of their thermo-mechanical behavior. The glass transition (T_g) temperature was determined from the temperature dependence of the DMA response, using the tan δ peak of the storage modulus drop in accordance with ASTM E1640 and ISO 6721.

RESULTS AND DISCUSSION

Morphological Evolution of the Irradiated Powder Bed

Figure 3 summarizes the progressive morphological evolution of the formulated micro-pellets in the powder bed during the microwave-irradiation cycle. **Figure 3** displays a schematic representation of the microstructural and morphological progress of the micro-pellets in the powder bed next to their corresponding SEM micrograph at four different stages of the cycle. The sequence clearly shows that the EM melt process proceeds through distinct stages, beginning with the "green" micro-pellets in the packed bed (Stage 1), followed by neck formation, inter-particle sintering (Stage 2), "neck" growth, particle coalescence and bonding (Stage 3), and ending up in the development of a more fused and continuous segregated nanocomposite structure (Stage 4). This progression is consistent with a thermally activated fusion mechanism in which microwave energy is converted locally into heat from the EM-susceptible CNT network, producing interfacial softening, sintering, and finally fusion across the whole bed area that is being irradiated [10].

In Stage 1, the powder bed consists of discrete CNT-coated polymer micro-pellets of irregular shapes (i.e., due to the cryogenic micronization recycling process) but with clearly defined boundaries and of a similar size of around 100 μm. The schematic shows more uniform micro-pellets for the sake of clarity. This state is characteristic of the initial irradiation stage, where the thermal input is still insufficient to activate the interparticle bonding processes required for neck formation and particle coalescence [35].

Stage 2 represents the onset of EM coupling, heating, and "neck" formation between pellets. At this stage, localized energy absorption at the CNT network produces softening at the micro-pellets' surface, allowing adjacent particles to make stronger contact and form interparticle necks into a sintered structure. Both the schematic and SEM indicate that the pellets begin to lose their sharp individuality, while small bonding bridges appear at the contact points. This is a critical transition in the fusion process, because neck growth marks the onset of thermally driven inter-pellet bonding and of material transport between adjacent particles [36]. The formation of these necks implies that microwave-induced lossy processes are sufficient to transfer energy farther away from the CNT network interfacial regions, initiating inter-pellet sintering without yet causing complete collapse of particle identity.

As irradiation continues, Stage 3 shows pronounced particle coalescence, fusion, and melting. The boundaries between neighboring pellets become less distinct, and the material begins to behave as a continuous connected structure rather than a collection of separate entities. SEM reveals a much smoother and more fused morphology, indicating that the interparticle necks have grown substantially and that surface tension-driven flow has promoted consolidation. At this point, the system transitions from a sintered to a more integrated structure, which is essential for achieving mechanical continuity and improved adhesion. The disappearance of most particle boundaries suggests that the thermal field is now sufficient to drive widespread interfacial melting and coalescence. Moreover, the viscoelastic deformation

of the original micro-pellets also distorts the original “green” CNT network, and as a consequence, as discussed in the transport properties section, the electrical conductivity of the green bed gets significantly reduced, leading to a reduction in EM susceptibility in the resulting fused layer. This is beneficial for the SMM process, as subsequent layers spread on top of the previous ones will be more EM-susceptible than the one underneath, yielding enough layer selectivity during the irradiation process.

Stage 4 corresponds to the melting and fusion of the irradiated section of the bed and to the formation of a largely “homogeneous” structure. The schematic shows that the original pellets’ boundaries are nearly absent, leaving only a continuous structure with residual pores/voids, and in some cases, well-defined CNT-rich interphase regions and CNT remaining clusters. SEM supports this interpretation by displaying a dense, continuous morphology with much less visible particle individuality. However, the remaining pores indicate that full microstructural continuity is not always achieved (depending on irradiation conditions and bed characteristics). These pores/voids may originate from several reasons, such as incomplete collapse of inter-pellets voids, trapped air, gas products from local polymer degradation, local viscoelastically impeded flow, and even from polymer solidification and crystallization processes [ref].

Taken together, these four stages provide direct evidence that the bed consolidation mechanism during irradiation is governed by a progressive thermal evolution from individual particles to sintering, fusion, and even melting. The microstructural sequence is especially important because it connects the macroscopic heating and layer formation process to localized EM coupling and microscopic inter-particle mechanisms. In particular, the microstructural evolution suggests that microwave-responsive powder bed feedstocks can convert EM energy into localized interfacial heating, enabling inter-particle fusion at relatively early stages, promoting structural continuity. This mechanistic understanding is necessary to demonstrate

the potential of EM melt processing of thermoplastics in innovative future AM technologies, such as SMM and SMS, capable of dealing with HP and functional thermoplastic materials.

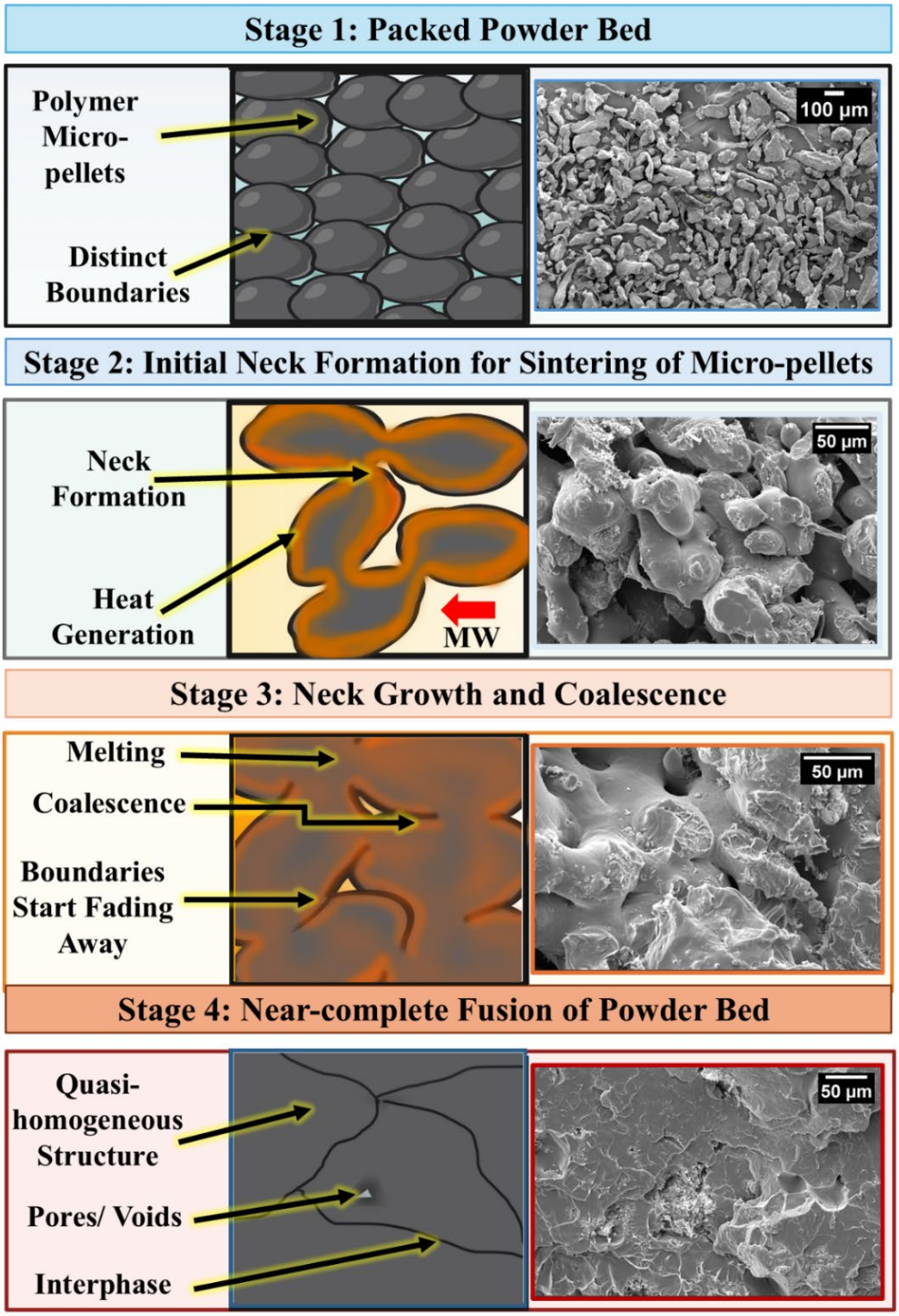

Figure 3. Schematic representation and corresponding electron micrographs of the morphological evolution of the EM-susceptible CNT/rPPS powder bed during irradiation: **Stage 1**, powder bed of CNT-coated micro-pellets spread and packed; **Stage 2**, initial "neck" formation and sintering between adjacent pellets under irradiation; **Stage 3**, neck growth, particle coalescence, and boundary fading; and **Stage 4**, near-complete fusion and melting of the powder bed into a "quasi-homogeneous" microstructure with tolerable levels of residual pores/voids content and a CNT-rich network at the interphase regions.

Microstructure and Morphology of the SMM Specimens

Figure 4 shows the SEM micrographs of the cross-section of the 3-layer SMM specimens. As **Figures 4a** and **4b** reveal, the specimen structure is clearly layered and exhibits excellent interlayer bonding and integrity, as evidenced by the absence of obvious delamination across layers 1, 2, and 3. As expected, instead of an entirely dense cross-section structure, **Figure 4a** displays some micro-voids and localized defects, suggesting substantial but incomplete consolidation. The irregular geometry of the rPPS micro-pellets may also likely contribute to micro-void formation when the powder bed displays more limited packing efficiency, and when residual inter-pellet gaps and interstices become more prominent [37]. Some of these micro-voids are concentrated near the interlayer regions, suggesting that porosity is more likely to form preferentially at the layer interfaces.

Figure 4b displays the cross-section of another specimen at larger magnification, also showing excellent interlayer bonding. The SMM powder bed fusion approach relies on the differential EM response between the top green layer and the previous, less EM-susceptible "sintered" layers. This enables a good level of selective melting, which promotes such a strong interlayer bonding [31]. This behavior is consistent with the observation that, after a layer undergoes melting, its electromagnetic susceptibility decreases due to the restructuring, redistribution, and partial embedding of CNTs within the polymer matrix [32]. As the previously processed layer becomes less microwave-responsive, microwave energy is increasingly absorbed by the top green layer, allowing sequential layer fusion without severe overheating of the underlying structure. In this manner, the spatial heating distribution is governed primarily by the intrinsic material response and the engineered nanoparticle-micro-pellet interphase distribution rather than by solely the external EM beam. Some residual micro-voids remained because the irradiation time and energy input were inadequate to eliminate

porosity entirely [38]. Moreover, good interfacial softening and chain interdiffusion between adjacent layers can be observed [31,35].

Figures 4c through **4f** show a good level of morphological segregation with remaining CNT agglomerates in the pellets' interphase regions, forming the network that yields the final transport properties in the specimens. These CNT-rich regions are the regions serving as electromagnetically active pathways. Overall, the microstructure demonstrates successful interlayer bonding and vertical consolidation but also indicates that further optimization of exposure time, powder deposition, and bed characteristics is required to reduce porosity and improve structural uniformity.

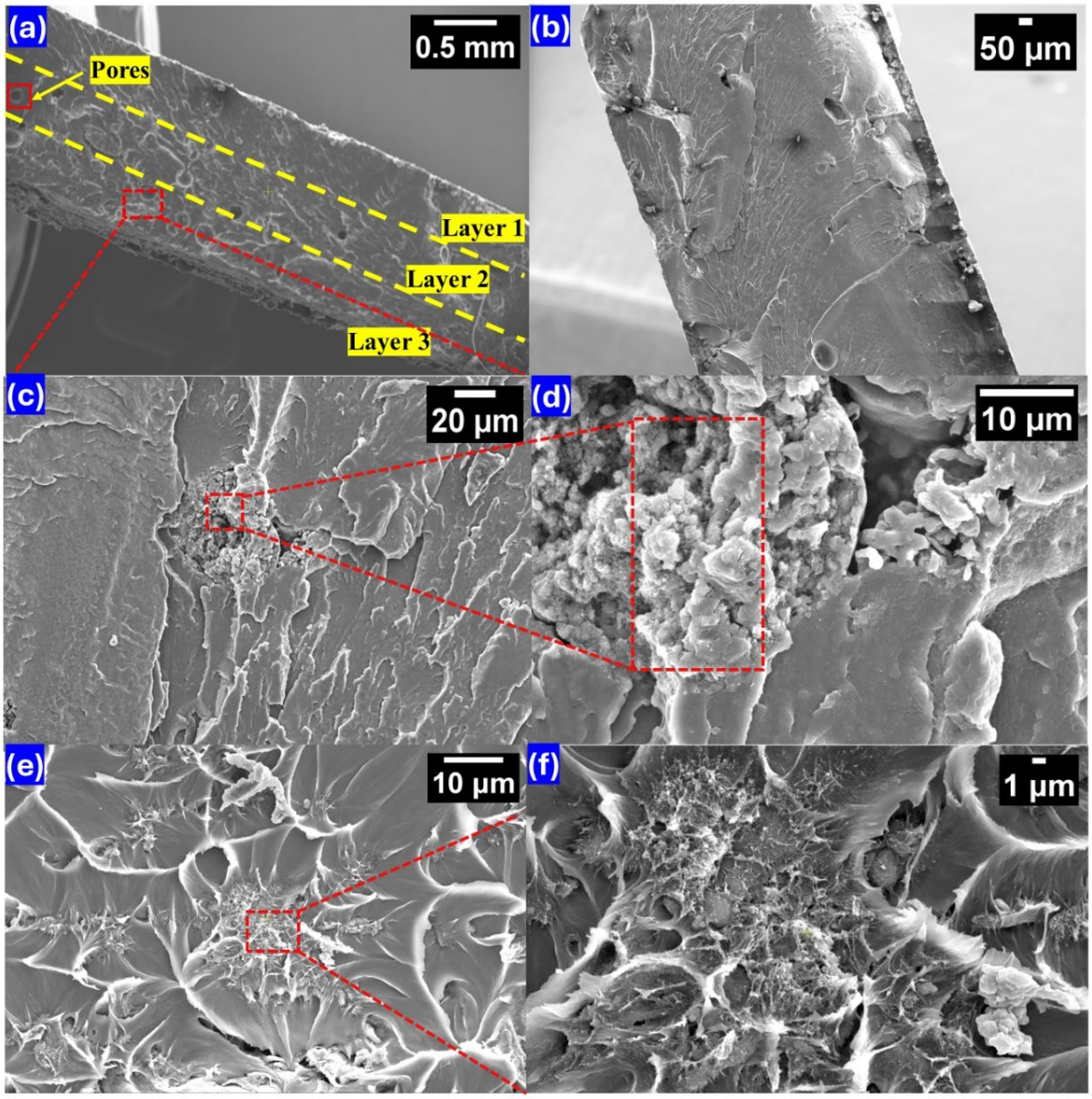

Figure 4. SEM micrographs of the cross-section of the SMM powder bed fusion specimens at different magnifications: (a, b) low magnification(×50), showing the overall layered structure; (c, d) intermediate magnification; and (e, f) high magnification, revealing the fused microstructure, micro-voids, CNT agglomerates, and CNT-rich networks at interphase regions of the segregated composite material.

Electrical Conductivity of the SSM Specimens

Figure 5 shows that the SMM specimens exhibit anisotropic electrical conductivity. Their conductivity reaches $(3.13\pm0.85)\times10^{-8}$ S/m and $(2.97\pm0.35)\times10^{-11}$ S/m in the in-plane direction and the through-plane direction, respectively. The in-plane value is three orders of magnitude higher than that of neat rPPS at $(2.760 \pm 0.523)\times10^{-11}$ S/m; whereas the through-plane value is

statistically not different from the rPPS resin value. Furthermore, the conductivity of the formulated green powder measured prior to SMM processing yielded a value of $(1.590 \pm 0.383) \times 10^{-6}$ S/m. These results indicate that upon irradiation, the conductivity of the powder bed decreases by nearly 2 orders of magnitude. This mainly occurs because, during SMM processing, the CNTs become engulfed by the viscoelastic polymer matrix, which disrupts the conductive network pathways to some extent [10].

The anisotropy displayed by the specimens may be attributed to selective microwave coupling with CNT-rich regions during irradiation, which generates localized heating at inter-pellet interfaces and promotes fusion without complete bulk "homogenization". Under these conditions, charge transport likely occurs through direct CNT-CNT contacts at fused interfaces and via tunneling across residual gaps, consistent with percolation-controlled transport in nanocomposites [39]. Moreover, the limited but existing in-plane viscoelastic flow of each layer as it is irradiated may also contribute to some anisotropy. As a result, conductive pathways are formed primarily through discrete CNT bridges at pellet-pellet contacts, rather than through a continuous, fully percolated CNT network [40].

Furthermore, the observed results suggest the formation of a directionally biased conductive network, where microwave-induced localized heating retains CNT-rich pathways at interfacial regions but incomplete vertical connectivity limits through-thickness transport (**Figure 5**), resulting in a lower conductivity [32]. During the irradiation of the powder bed, conductivity is strongly influenced by packing density, interparticle contact quality, residual porosity, and incomplete interfacial fusion, all of which increase contact resistance and the tunneling distance, thereby hindering long-range charge transport [41,42]. This behavior is consistent with percolation theory, which predicts a strong dependence of conductivity on network connectivity [43,44].

In SLS studies, Lupone et al. reported that carbon-fiber-reinforced composites exhibited higher electrical conductivity than graphite-filled systems. At the same time, hybrid formulations were reported to show intermediate behavior and a percolation threshold in the range of 15-20 wt% reinforcement [45]. In contrast, in the present work, the conductivity levels achieved at only 1 wt% CNT indicate efficient network formation at very low CNT loading levels, highlighting the potential of our team's method to formulate an EM-susceptible powder bed for the fabrication of functional nanocomposite parts with reduced nanoparticle content. Moreover, compared with other conventional powder bed fusion routes, SSM powder bed fusion may retain a more segregated but percolated microstructure because the localized microwave heating promotes very sharp pellet-pellet and CNT-polymer interfacial fusion as well as higher CNT networking. We acknowledge that further optimization of powder packing, CNT dispersion, and microwave-field uniformity will be important for improving interparticle connectivity, reducing porosity, micro-voids, and contact resistance, and, in general, achieving better transport and mechanical properties.

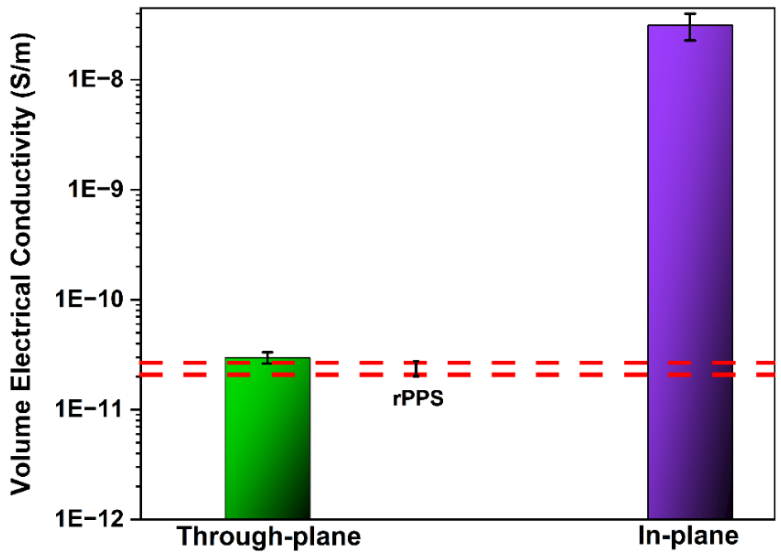

Figure 5. Through-plane and in-plane volume electrical conductivity of the SMM specimens. Error bars represent 95% confidence intervals.

Dielectric Properties of the SMM Specimens

Figure 6 displays the AC dielectric response of the SMM specimens from 100 Hz to 200 kHz. The dielectric properties, electrical real relative permittivity ($\varepsilon'/\varepsilon_0$) and imaginary relative permittivity (or dielectric loss, $\varepsilon''/\varepsilon_0$) exhibit a strong frequency dependence. As shown in **Figure 6**, at low frequencies (100 Hz near the DC regime), the real relative permittivity reaches $(6.06\pm1.69)\times10^6$, reflecting a pronounced interfacial charge accumulation at CNT-polymer boundaries due to the conductivity mismatch between the CNT-rich phase and the insulating polymer matrix, which leads to Maxwell-Wagner-Sillars polarization [46]. The CNT/rPPS interface, therefore, behaves as a capacitor-like region storing charge under a low-frequency electric field [46]. With increasing frequency, $\varepsilon'/\varepsilon_0$ decreases sharply to $(5.33\pm3.15)\times10^2$ at 10 kHz and then to $(4.43\pm0.41)\times10^1$ at 100 kHz and $(3.95\pm0.24)\times10^1$ at 200 kHz. This decay occurs because the interfacial charges cannot respond rapidly enough to the alternating field, thereby suppressing space-charge polarization and increasing lossy transport processes [47].

A similar trend is observed in the imaginary relative permittivity, $\varepsilon''/\varepsilon_0$, in **Figure 6**, which is very high $(8.76\pm3.39)\times10^9$ at a low frequency of 100 Hz, and decreases quickly down to $(8.81\pm4.07)\times10^0$ at 200 kHz. This behavior suggests that energy dissipation is dominated by interfacial polarization and conduction-related loss associated with charge hopping and leakage across CNT junctions. The persistence of dielectric loss across the measured range indicates that the CNT network is electrically active, while the sharp decay with frequency reflects the limited ability of space charge to follow the alternating field [48,49]. Moreover, the dielectric data are consistent with the conductivity results, which indicate that the CNT network is electrically active but spatially discontinuous, giving rise to partial percolation and anisotropic transport. In such systems, the same interfacial barriers and tunneling gaps that limit long-range conduction also enhance low-frequency dielectric dispersion and contribute to AC loss through

hopping and leakage-current pathways [49,50]. Thus, the strong low-frequency real relative permittivity and the persistence of dielectric loss over the measured range suggest that the SMM powder bed fusion generates a heterogeneous microstructure (segregated) with extensive interfacial area, where charge accumulation dominates at low frequency but increasingly transitions to dissipative transport as frequency rises.

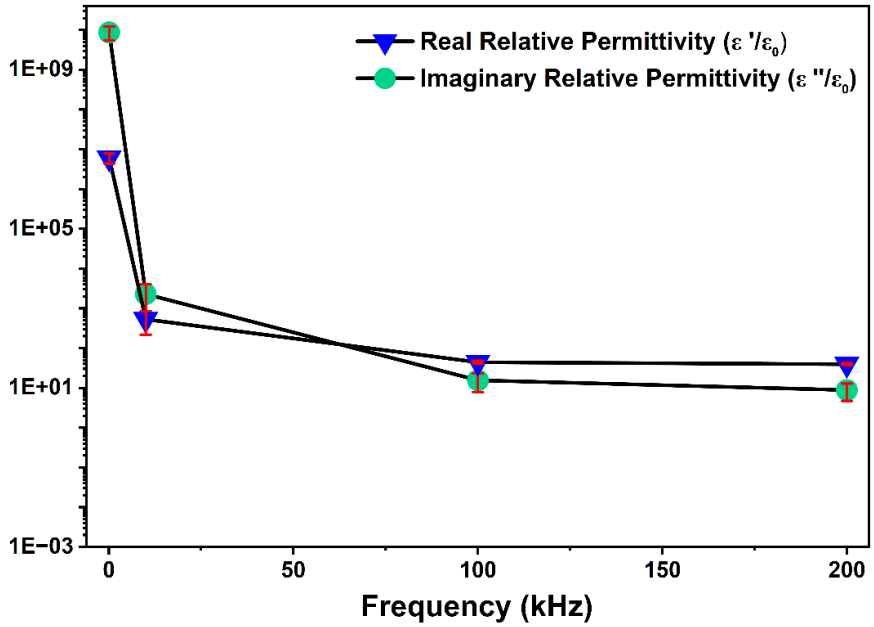

Figure 6. Frequency-dependent dielectric response ($\varepsilon'/\varepsilon_0$ and $\varepsilon''/\varepsilon_0$) of the SMM specimens.

Mechanical Properties of the SMM Specimens

The average values of Young's modulus, tensile strength, and strain-at-break obtained from tensile testing for the SMM specimens are shown in **Figure 7**. These results collectively demonstrate that SSM powder bed fusion produces mechanically functional, robust structures rather than loosely bonded or partially fused powder/structures. The tensile strength (**Figure 7a**) average value of 52.61 ± 9.16 MPa further confirms that the nanocomposite material can withstand substantial load before failure. This level of strength is about 20% higher than, but statistically similar to, neat rPPS (44.56 ± 3.77 MPa). Nevertheless, the data set displays more

variability than that of the rPPS. This is probably due to the presence of micro-voids in the SMM specimens. This acceptable strength level arises from the combined effects of matrix consolidation, inter-pellet bonding and fusion, and likely, CNT-mediated reinforcement [51]. In CNT-reinforced polymer systems, such improvements are typically governed by (i) efficient stress transfer across the CNT-matrix interface, (ii) the formation of interconnected CNT networks that constrain deformation, and (iii) nanoscale stress redistribution that mitigates localized failure [52,53]. In the present system, CNTs embedded within the EM-structured network likely act as mechanical bridges between adjacent rPPS micro-domains, facilitating stress transfer across fused interfaces. Although inter-pellet fusion is not fully complete all across, and some voids may weaken the structure, these interactions provide a clear basis for the observed reinforcing effect. The relatively high tensile strength at low CNT loading highlights the effectiveness of the EM-induced structuring approach in promoting reinforcement without requiring high filler concentrations.

As shown in **Figure7b**, the elastic modulus of 1573.1 ± 3.87 MPa is particularly notable and remained within the same range as that of the neat polymer, indicating resistance to elastic deformation and suggesting also an efficient load transfer within the consolidated structure [54,55]. This behavior is consistent with a percolated or semi-percolated CNT network, which enhances stiffness by restricting polymer chain mobility and reinforcing the matrix through effective interfacial interactions [55–57]. Once again, the SMM stiffness was not significantly different from that of the rPPS but showed more statistical variability.

As displayed in **Figure 7c,** a strain-at-break of 4.79 ± 2.46% of the SMM specimens provides valuable insight into their failure mechanisms. This value is statistically not different from the ductility of the neat rPPS (3.09 ± 0.31%). In CNT/polymer systems, strain-at-break often decreases after CNT addition, which may be interpreted as evidence that plastic yielding in the fractured zone is reduced relative to the neat polymer [58]. This response is characteristic

of a microstructure governed by interfacial failure between partially fused particles, rather than a fully continuous polymer phase. Residual interfaces and micro-voids formed during the SSM powder bed fusion process likely act as stress concentrators, restricting elongation and promoting premature failure [59]. Nevertheless, despite these structural defects, the SMM specimens display quite acceptable mechanical properties, comparable or even superior to the rPPS matrix.

From a process-structure-property perspective, the mechanical response of the SMM specimens is consistent with a localized interfacial activation mechanism [31]. In our SMM process that irradiates the whole specimen (without a focused microwave beam or MASER), microwave energy may lead to some hot-spots but still selectively heats CNT-rich percolated regions, promoting bonding at inter-pellet contacts without requiring full bulk melting or external compaction. While this enables energy-efficient pellet fusion and preservation of the CNT architecture, it also limits densification and microstructural uniformity to some extent compared to conventional SLS techniques that focus energy [60]. Despite this, the present results demonstrate that our preliminary SSM technique (even without a focused beam) can rapidly produce high-performance nanocomposite parts (i.e., with polymers of high melting point) of simple geometries with adequate stiffness and strength. This supports the feasibility of SMM powder bed fusion as an alternative, potential, and future AM technology. We acknowledge that we are proposing an AM conceptualization only, and that much needs to be done (such as further optimization of powder formulation, irradiation conditions, microwave energy delivery, microwave beam focusing, and electromechanical automation of the energy deposition and of the powder bed spreading system) to achieve high-performance components of complex shapes. Nonetheless, these findings introduce SSM powder bed fusion as a potential AM route for HP functional thermoplastic parts, useful in electronics, aerospace, space, and military applications.

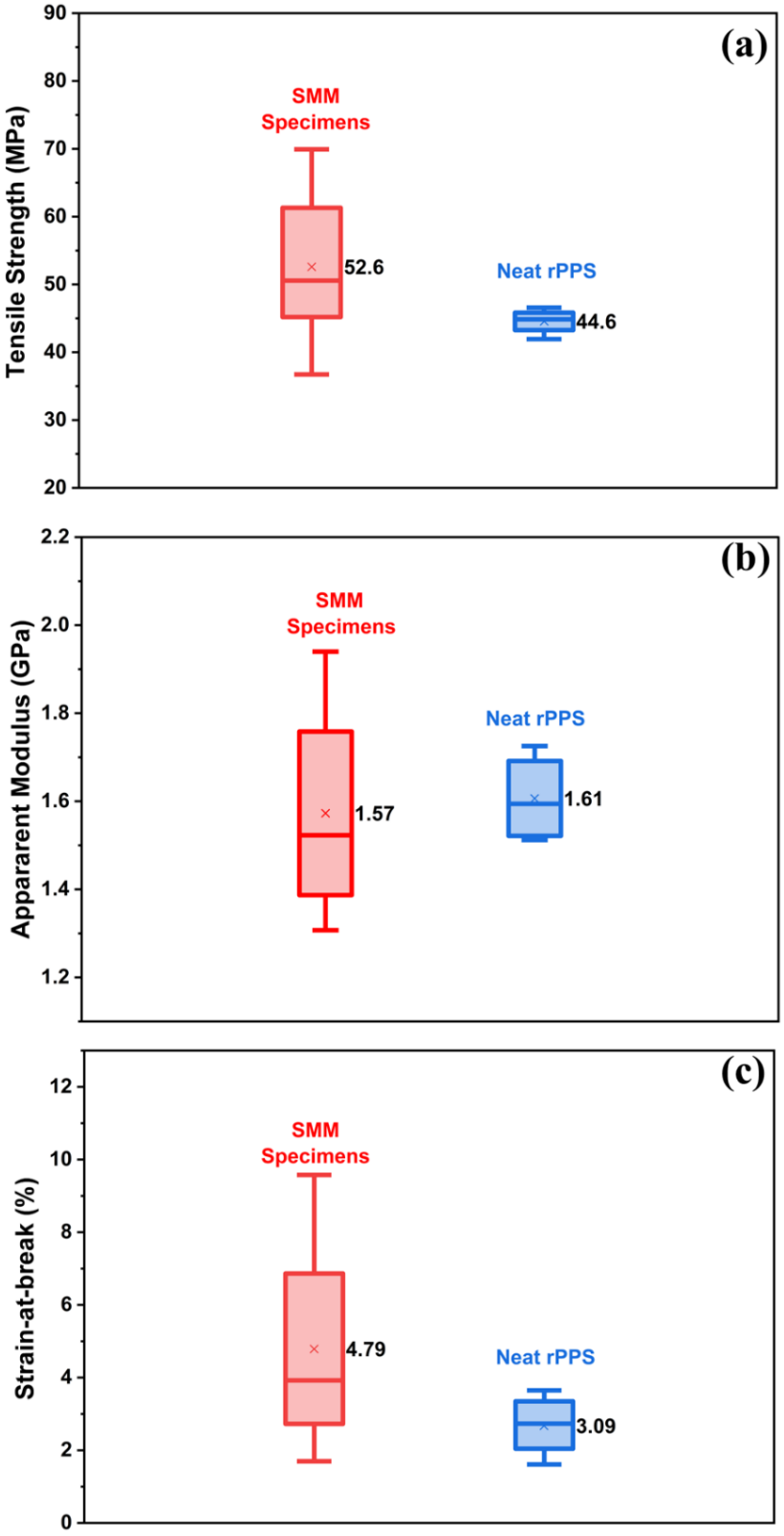

Figure 7. Data distribution of the tensile mechanical properties of the SMM specimens: (a) tensile strength, (b) modulus, and (c) strain-at-break.

Dynamic Mechanical Analysis of the SMM Specimens

Figure 8 displays the representative viscoelastic dynamic mechanical behavior of the SMM specimens and that of the neat rPPS. The temperature-dependent storage modulus (E'), loss modulus (E''), and damping factor (tan δ) are displayed. As shown in **Figure 8a**, in the glassy region, the SSM specimens exhibit a similar storage modulus (E') to that of the neat rPPS (**Figure 8b**), indicating a similar response at room temperature [61]. As shown in **Figure 8a**, the magnitude of the storage modulus in this region (of the order of ~1-2 GPa) is consistent with the tensile modulus values from quasi-static tensile testing (1573.1 ± 3.87 MPa), confirming the effect of the CNT network across both static and dynamic loading conditions [62]. As temperature increases, both the SMM specimens and the neat rPPS exhibit a gradual decrease in storage modulus corresponding to the onset of segmental motion in the polymer matrix [63]. However, the SSM specimens show a sharper leathery transition, but a more gradual decay of the rubbery plateau. The CNT network, which may yield a pseudo-crosslinking effect, may be responsible for this behavior of the rubbery plateau, as this region is governed by entanglements of long-chain molecules and networks, while micro-voids may be leading the sharp leathery transition [62]. This is consistent with the tan δ-derived glass transition temperature (T_g), which for the SMM specimens is 132.36 °C and 136.05 °C for neat rPPS. This modest downward shift suggests that, although CNTs contribute to stiffness, relaxation behavior is also influenced by microstructural heterogeneity introduced during the SSM process [64]. Residual interfaces, incomplete fusion, and localized regions of increased free volume may promote earlier segmental relaxation in some parts of the material [64,65]. As noted by Khan et al., strong nanoparticle-polymer interactions can restrict chain diffusion, whereas localized free-volume-rich regions associated with imperfect consolidation may facilitate earlier relaxation, leading to a net reduction in T_g consistent with free-volume-based interpretations of polymer behavior [66]. To a lesser extent, possible thermally induced degradation in the polymer network may

also contribute to this shift. Overall, the nanocomposite response reflects a balance between CNT-mediated stiffening and EM-induced heterogeneity and defects rather than a simple increase in T_g.

When considered alongside the tensile results, the DMA data confirm that SSM fusion produces parts with retained stiffness, very good strength, and constrained viscoelastic relaxation behavior. The tensile response demonstrates load-bearing capability under static conditions, while the DMA results show that SMM specimens retain consistent thermomechanical behavior. Compared to neat rPPS, the SSM specimens exhibit improved elastic retention and reduced damping, supporting the conclusion that the EM-induced structuring attained via SMM generates a physically interconnected network that not only yields transport properties but also mechanical performance.

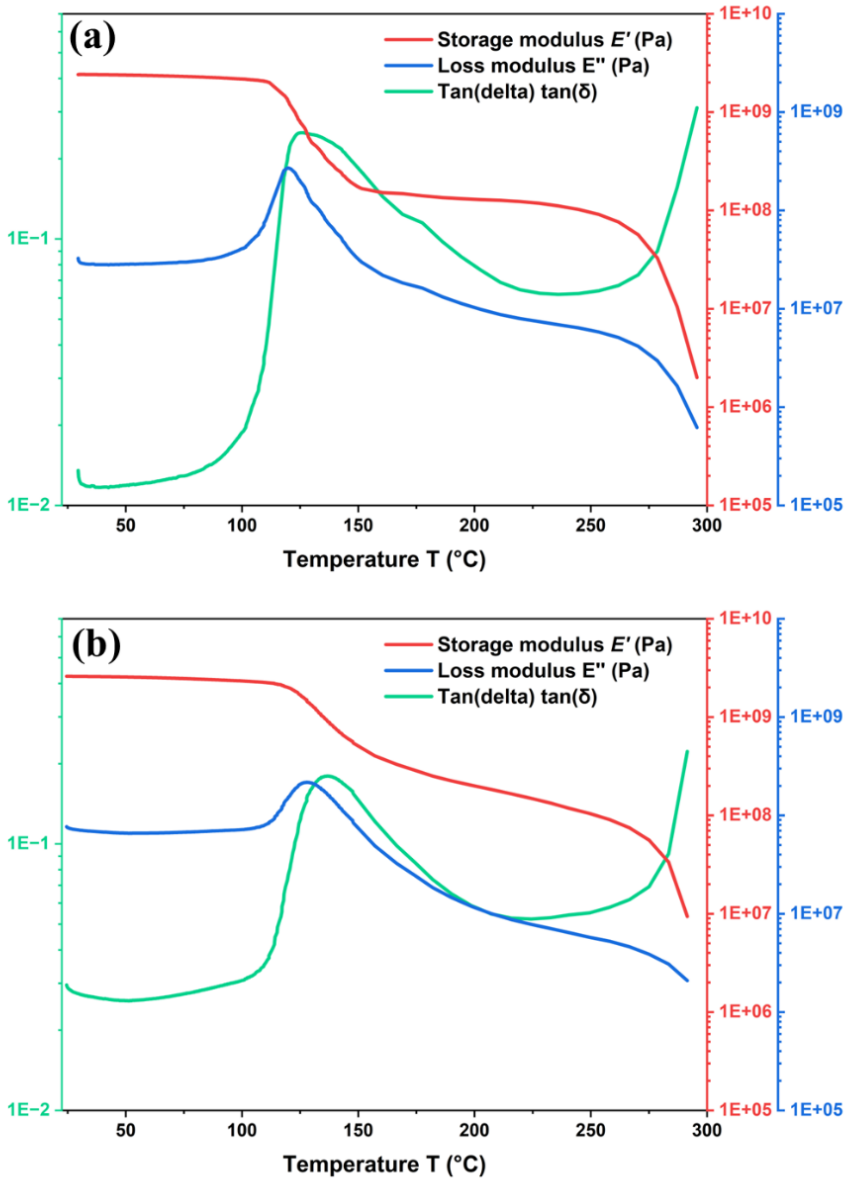

Figure 8. Dynamic viscoelastic response showing the thermomechanical behavior of the storage and loss moduli, as well as the loss tangent for (a) the SMM specimens and (b) for the neat rPPS.

CONCLUSIONS

This study underscores the potential of electromagnetic (EM) melt processing of thermoplastics as a basis for innovative additive manufacturing (AM) technologies that may yield high-performance (HP) thermoplastic parts with advanced functional and mechanical properties. In this work, we apply the EM melt processing to a powder bed fusion AM concept that uses microwaves to manufacture simple parts layer-by-layer. We call this conceptual manufacturing approach "selective microwave melting (SMM) or sintering (SMS)". This approach is not only innovative but may broaden the material scope for AM to high-performance (HP) thermoplastics and many other engineering thermoplastics, currently unavailable in AM. It may also open new pathways for sustainable, efficient, and versatile AM, driving forward the next generation of AM technologies. Thus, simple SMM specimens, made of a formulated powder bed consisting of CNT-coated recyclable polyphenylene sulfide (rPPS) micro-pellets (at 1 wt% CNT), exhibited a tensile strength of 52.61 ± 9.16 MPa, an excellent strength compared to the matrix resin, as well as excellent retention of stiffness and ductility. Dynamic mechanical analysis confirmed the thermomechanical properties of the SMM specimens. Microstructural analysis revealed an excellent interlayer bonding, CNT-rich interphases, and residual porosity and CNT aggregates, indicating an acceptable level of fusion, defects, consolidation, and CNT networking. Thus, electrical conductivity and dielectric measurements revealed pronounced anisotropy and a marked increase in conductivity and dielectric loss at low CNT loading, confirming the partial retention of electrically active networks during the SMM process. Collectively, this validates the feasibility of conceptual microwave-based powder bed fusion AM technologies. Moreover, these electromagnetic field-enabled AM methods present scalable, energy-efficient, and material-versatile pathways to fabricate the next generation of functional HP thermoplastic parts. The findings in this study

establish a conceptual foundation for expanding field-directed AM technologies that will enable a broader class of engineering and high-performance polymers and functional properties, offering exciting new possibilities in electronics, aerospace, space, energy, military, and sustainable manufacturing sectors.

ACKNOWLEDGEMENTS

This work was supported by a National Aeronautics and Space Administration (NASA) cooperative Agreement [Award No. 80NSSCM0041].

***Disclaimer Statement**:* "The material contained in this document is based upon work supported by a National Aeronautics and Space Administration (NASA) cooperative agreement. Any opinions, findings, conclusions, or recommendations expressed in this material are those of the author and do not necessarily reflect the views of NASA."

REFERENCES

[1] D. Ponnamma, Y. Yin, N. Salim, J. Parameswaranpillai, S. Thomas, N. Hameed, Recent progress and multifunctional applications of 3D printed graphene nanocomposites, Compos. Part B 204 (2021) 108493. https://doi.org/10.1016/j.compositesb.2020.108493.

[2] B. Hüner, M. Klstl, S. Uysal, İ.N. Uzgören, E. Özdoğan, Y.O. Süzen, N. Demir, M.F. Kaya, An Overview of Various Additive Manufacturing Technologies and Materials for Electrochemical Energy Conversion Applications, ACS Omega 7 (2022) 40638–40658. https://doi.org/10.1021/acsomega.2c05096.

[3] D.E.P. Klenam, F. McBagonluri, T.K. Asumadu, S.A. Osafo, M.O. Bodunrin, L. Agyepong, E.D. Osei, D. Mornah, W.O. Soboyejo, Additive manufacturing: shaping the future of the manufacturing industry – overview of trends, challenges and opportunities,

Appl. Eng. Sci. 22 (2025) 100224. https://doi.org/10.1016/j.apples.2025.100224.

[4] L. Zhou, J. Miller, J. Vezza, M. Mayster, M. Raffay, Q. Justice, Z. Al Tamimi, G. Hansotte, L.D. Sunkara, J. Bernat, Additive Manufacturing: A Comprehensive Review, Sensors 24 (2024). https://doi.org/10.3390/s24092668.

[5] L. Chanraksmey, B. Nie, W. Zhao, K. Thummavichai, Y. Chen, B. Chen, Additive manufacturing of functional high-performance polymers for energy storage, conversion, and insulation systems, Smart Mater. Manuf. 4 (2026) 100121. https://doi.org/10.1016/j.smmf.2025.100121.

[6] Á. Díaz-García, J.Y. Law, M. Felix, A. Guerrero, V. Franco, Functional, thermal and rheological properties of polymer-based magnetic composite filaments for additive manufacturing, Mater. Des. 219 (2022). https://doi.org/10.1016/j.matdes.2022.110806.

[7] C. Ye, C. Zhang, J. Zhao, Y. Dong, Effects of Post-processing on the Surface Finish, Porosity, Residual Stresses, and Fatigue Performance of Additive Manufactured Metals: A Review, J. Mater. Eng. Perform. 30 (2021) 6407–6425. https://doi.org/10.1007/s11665-021-06021-7.

[8] T. Siripongpreda, V.P. Hoven, B. Narupai, N. Rodthongku, Emerging 3D printing based on polymers and nanomaterial additives: Enhancement of properties and potential applications, Eur. Polym. J. 184 (2023) 111806. https://doi.org/10.1016/j.eurpolymj.2022.111806.

[9] A. Al Rashid, S.A. Khan, S. G. Al-Ghamdi, M. Koç, Additive manufacturing of polymer nanocomposites: Needs and challenges in materials, processes, and applications, J. Mater. Res. Technol. 14 (2021) 910–941. https://doi.org/10.1016/j.jmrt.2021.07.016.

[10] M. Mohoppu, U. Ayan, J. Schwartz, A. Al-Ostaz, M.G. Ucak-Astarlioglu, B.S. Villacorta, Carbon Nanotube-Based Segregated Thermoplastic Nanocomposites Structured via Electromagnetic Melt Processing, ACS Omega 9 (2024) 48546–48562.

https://doi.org/10.1021/acsomega.4c07372.

[11] T.P. Naik, I. Singh, A.K. Sharma, Processing of polymer matrix composites using microwave energy : A review, Compos. Part A 156 (2022) 106870. https://doi.org/10.1016/j.compositesa.2022.106870.

[12] Y. Hu, Recent progress in field-assisted additive manufacturing: Materials, methodologies, and applications, Mater. Horizons 8 (2021) 885–911. https://doi.org/10.1039/d0mh01322f.

[13] R.R. Mishra, A.K. Sharma, Microwave-material interaction phenomena: Heating mechanisms, challenges and opportunities in material processing, Compos. Part A Appl. Sci. Manuf. 81 (2016) 78–97. https://doi.org/10.1016/j.compositesa.2015.10.035.

[14] Y. Xie, J. Tang, F. Ye, P. Liu, Microwave-Assisted Sintering to Rapidly Construct a Segregated Structure in Low-Melt-Viscosity Poly(Lactic Acid) for Electromagnetic Interference Shielding, ACS Omega 5 (2020) 26116–26124. https://doi.org/10.1021/acsomega.0c03704.

[15] P. Goyal, S. Borkar, S. Bagade, O. Gorakh, N. Chandra, Green Processing of Materials with Microwaves, Mater. Process. 1 (2023) 9–13.

[16] F. Hossain, J. V. Turner, R. Wilson, L. Chen, G. de Looze, S.W. Kingman, C. Dodds, G. Dimitrakis, State-of-the-art in microwave processing of metals, metal powders and alloys, Renew. Sustain. Energy Rev. 202 (2024) 114650. https://doi.org/10.1016/j.rser.2024.114650.

[17] R. Guo, Y. Li, Q. Wang, Selective Microwave Sintering for Preparation of Organic Fiber Network-Reinforced Thermoplastic Composites, J. Appl. Polym. Sci. (2026) e70814. https://doi.org/https://doi.org/10.1002/app.70814.

[18] R.J.N. Joshua, S.A. Raj, M.T. Hameed Sultan, A. Łukaszewicz, J. Józwik, Z. Oksiuta, K. Dziedzic, A. Tofil, F.S. Shahar, Powder Bed Fusion 3D Printing in Precision

Manufacturing for Biomedical Applications: A Comprehensive Review, Materials (Basel). 17 (2024) 1–30. https://doi.org/10.3390/ma17030769.

[19] J. Zou, S. Xie, B. Zhu, T. Liu, C. Fang, Y. Zhuang, Effect of material surface states in the laser spot on the absorptivity during laser melting processing, Appl. Surf. Sci. 688 (2025) 162384. https://doi.org/10.1016/j.apsusc.2025.162384.

[20] C. Meier, R. Weissbach, J. Weinberg, W.A. Wall, A.J. Hart, Critical influences of particle size and adhesion on the powder layer uniformity in metal additive manufacturing, J. Mater. Process. Technol. 266 (2019) 484–501. https://doi.org/10.1016/j.jmatprotec.2018.10.037.

[21] C.Y. Yap, C.K. Chua, Z.L. Dong, Z.H. Liu, D.Q. Zhang, L.E. Loh, S.L. Sing, Review of selective laser melting: Materials and applications, Appl. Phys. Rev. 2 (2015). https://doi.org/10.1063/1.4935926.

[22] R.J.R. Hayward, M. Valentin, M. Olivier, G.D.S. Smart, Microwave and optical masers, 27 (1964) 241. https://doi.org/10.1088/0034-4885/27/1/306.

[23] J.P. Gordon, P. Gordon, THE MASER, 199 (1958) 42–51. https://doi.org/https://www.jstor.org/stable/24944848.

[24] P.H.M. Putra, S. Rozali, M.F.A. Patah, A. Idris, A review of microwave pyrolysis as a sustainable plastic waste management technique, J. Environ. Manage. 303 (2022) 114240. https://doi.org/10.1016/j.jenvman.2021.114240.

[25] J. Guo, Y. Liu, R. Prada-Silvy, Y. Tan, S. Azad, B. Krause, P. Pötschke, B.P. Grady, Aspect ratio effects of multi-walled carbon nanotubes on electrical, mechanical, and thermal properties of polycarbonate/MWCNT composites, J. Polym. Sci. Part B Polym. Phys. 52 (2014) 73–83. https://doi.org/https://doi.org/10.1002/polb.23402.

[26] F. Choudhary, P. Mudgal, A. Parvez, P. Sharma, H. Farooqi, A review on synthesis, properties and prospective applications of carbon nanomaterials, Nano-Structures and

Nano-Objects 38 (2024) 101186. https://doi.org/10.1016/j.nanoso.2024.101186.

[27] M. Adam, N. Hjalmarsson, C.S. Lee, D.J. Irvine, J. Robinson, E. Binner, Understanding microwave interactions with polymers to enable advanced plastic chemical recycling, Polym. Test. 137 (2024) 108483. https://doi.org/10.1016/j.polymertesting.2024.108483.

[28] R.R. Mishra, A.K. Sharma, Composites : Part A Microwave – material interaction phenomena : Heating mechanisms , challenges and opportunities in material processing, Compos. PART A 81 (2016) 78–97. https://doi.org/10.1016/j.compositesa.2015.10.035.

[29] E.W. Fenta, B.A. Mebratie, Advancements in carbon nanotube-polymer composites: Enhancing properties and applications through advanced manufacturing techniques, Heliyon 10 (2024) e36490. https://doi.org/10.1016/j.heliyon.2024.e36490.

[30] J. Hu, T. Yang, D. Wu, J. Zhang, Rapid fabrication of high strength PEEK/CNTs composites with segregated structure and weld repair through microwave sintering, Compos. Part A Appl. Sci. Manuf. 200 (2026). https://doi.org/10.1016/j.compositesa.2025.109333.

[31] M. Mohoppu, U. Ayan, S. Nouranian, A. Al-Ostaz, M.G. Ucak-Astarlioglu, B.S. Villacorta, Rapid Microwave Bonding of Thermoplastics Substrates with Electromagnetically Susceptible Graphene/Poly (ether ether ketone) Segregated Nanoformulates, ACS Appl. Eng. Mater. 3 (2025) 26683–2696. https://doi.org/https://doi.org/10.1021/acsaenm.5c00520.

[32] M. Mohoppu, U. Ayan, B. Kattel, O. Oulhakem, B.S. Villacorta, Morphology-driven electromagnetic shielding performance of graphitic nanoparticles in segregated polypropylene nanocomposites via electromagnetic melt processing, Compos. Commun. 60 (2025) 102614. https://doi.org/10.1016/j.coco.2025.102614.

[33] S. Singh, P. Hubert, Optimizing High-Performance Polyphenylene Sulfide–Polycarbonate Blends for Additive Manufacturing, ACS Appl. Eng. Mater. 3 (2025)

2051–2063. https://doi.org/10.1021/acsaenm.5c00240.

[34] A. Das, C.A. Chatham, J.J. Fallon, C.E. Zawaski, E.L. Gilmer, C.B. Williams, M.J. Bortner, Current understanding and challenges in high temperature additive manufacturing of engineering thermoplastic polymers, Addit. Manuf. 34 (2020) 101218. https://doi.org/10.1016/j.addma.2020.101218.

[35] C.A. Chatham, M.J. Bortner, B.N. Johnson, T.E. Long, C.B. Williams, Predicting mechanical property plateau in laser polymer powder bed fusion additive manufacturing via the critical coalescence ratio, Mater. Des. 201 (2021) 109474. https://doi.org/10.1016/j.matdes.2021.109474.

[36] P. Hejmady, C.A. Van Breemen, P.D. Anderson, Laser sintering of polymer particle pairs studied by in situ visualization †, (2019) 1373–1387. https://doi.org/10.1039/c8sm02081g.

[37] S.Z. Ajabshir, H. Mohammadkamal, Z.Z. Ajabshir, D. Barletta, F. Caiazzo, M. Poletto, Polymeric Powders for Powder Bed Fusion : From Chemistry and Powder Characteristics to Process Parameters , Defects and Applications, 18 (2026) 1–55. https://doi.org/https://doi.org/10.3390/polym18050622.

[38] A. Liebrich, H.C. Langowski, R. Schreiber, B.R. Pinzer, Porosity distribution in laser-sintered polymeric thin sheets as revealed by X-ray micro tomography, Polym. Test. 76 (2019) 286–297. https://doi.org/10.1016/j.polymertesting.2019.02.014.

[39] Z. Liu, W. Peng, Y. Zare, D. Hui, K.Y. Rhee, Predicting the electrical conductivity in polymer carbon nanotube nanocomposites based on the volume fractions and resistances of the nanoparticle, interphase, and tunneling regions in conductive networks, RSC Adv. 8 (2018) 19001–19010. https://doi.org/10.1039/c8ra00811f.

[40] K. Zhang, G.H. Li, L.M. Feng, N. Wang, J. Guo, K. Sun, K.X. Yu, J.B. Zeng, T. Li, Z. Guo, M. Wang, Ultralow percolation threshold and enhanced electromagnetic

interference shielding in poly(l-lactide)/multi-walled carbon nanotube nanocomposites with electrically conductive segregated networks, J. Mater. Chem. C 5 (2017) 9359–9369. https://doi.org/10.1039/c7tc02948a.

[41] M. Ahlskog, M. Haukka, Preparation of Highly Porous Carbonous Electrodes by Selective Laser Sintering¨, (2019). https://doi.org/10.1021/acsaem.8b01881.

[42] T. Tarlton, E. Sullivan, J. Brown, P.A. Derosa, The role of agglomeration in the conductivity of carbon nanotube composites near percolation, J. Appl. Phys. 121 (2017). https://doi.org/10.1063/1.4977100.

[43] X.M. Chen, J.W. Shen, W.Y. Huang, Novel electrically conductive polypropylene/graphite nanocomposites, J. Mater. Sci. Lett. 21 (2002) 213–214. https://doi.org/10.1023/A:1014708808230.

[44] B. Herren, P. Larson, M.C. Saha, Y. Liu, Enhanced electrical conductivity of carbon nanotube-based elastomer nanocomposites prepared by microwave curing, Polymers (Basel). 11 (2019). https://doi.org/10.3390/polym11071212.

[45] F. Lupone, E. Padovano, O. Ostrovskaya, A. Russo, C. Badini, Innovative approach to the development of conductive hybrid composites for Selective Laser Sintering, Compos. Part A 147 (2021) 106429. https://doi.org/10.1016/j.compositesa.2021.106429.

[46] X. Xia, Z. Zhong, G.J. Weng, Mechanics of Materials Maxwell – Wagner – Sillars mechanism in the frequency dependence of electrical conductivity and dielectric permittivity of graphene-polymer nanocomposites, Mech. Mater. 109 (2017) 42–50. https://doi.org/10.1016/j.mechmat.2017.03.014.

[47] X. Xia, Y. Wang, Z. Zhong, G.J. Weng, A frequency-dependent theory of electrical conductivity and dielectric permittivity for graphene-polymer nanocomposites, Carbon N. Y. 111 (2017) 221–230. https://doi.org/10.1016/j.carbon.2016.09.078.

[48] V.A. Online, R.B. Alam, M.R. Islam, Effect of MWCNT nanofiller on the dielectric

performance of bio-inspired gelatin based nanocomposites, 12 (2022) 14686–14697. https://doi.org/10.1039/d2ra01508k.

[49] H. Sun, H. Zhang, S. Liu, N. Ning, L. Zhang, Interfacial polarization and dielectric properties of aligned carbon nanotubes / polymer composites : The role of molecular polarity, Compos. Sci. Technol. 154 (2018) 145–153. https://doi.org/10.1016/j.compscitech.2017.11.008.

[50] H. Du, C. Fang, J. Zhang, X. Xia, G.J. Weng, Segregated carbon nanotube networks in CNT-polymer nanocomposites for higher electrical conductivity and dielectric permittivity, and lower percolation threshold, Int. J. Eng. Sci. 173 (2022) 103650. https://doi.org/10.1016/j.ijengsci.2022.103650.

[51] J.M. Zhu, Y. Zare, K.Y. Rhee, Analysis of the roles of interphase, waviness and agglomeration of CNT in the electrical conductivity and tensile modulus of polymer/CNT nanocomposites by theoretical approaches, Colloids Surfaces A Physicochem. Eng. Asp. 539 (2018) 29–36. https://doi.org/10.1016/j.colsurfa.2017.12.001.

[52] C. V. Opelt, D. Becker, C.M. Lepienski, L.A.F. Coelho, Reinforcement and toughening mechanisms in polymer nanocomposites - Carbon nanotubes and aluminum oxide, Compos. Part B Eng. 75 (2015) 119–126. https://doi.org/10.1016/j.compositesb.2015.01.019.

[53] A. Omrani, L.C. Simon, A.A. Rostami, The effects of alumina nanoparticle on the properties of an epoxy resin system, Mater. Chem. Phys. 114 (2009) 145–150. https://doi.org/10.1016/j.matchemphys.2008.08.090.

[54] B. Arash, Q. Wang, V.K. Varadan, Mechanical properties of carbon nanotube/polymer composites, Sci. Rep. 4 (2014) 1–8. https://doi.org/10.1038/srep06479.

[55] Y. Zare, K.Y. Rhee, A multistep methodology for calculation of the tensile modulus in

polymer/carbon nanotube nanocomposites above the percolation threshold based on the modified rule of mixtures, RSC Adv. 8 (2018) 30986–30993. https://doi.org/10.1039/C8RA04992K.

[56] S. Bagchi, A. Harpale, H.B. Chew, Interfacial load transfer mechanisms in carbon nanotube-polymer nanocomposites, Proc. R. Soc. A Math. Phys. Eng. Sci. 474 (2018). https://doi.org/10.1098/rspa.2017.0705.

[57] N.M. Nurazzi, F.A. Sabaruddin, M.M. Harussani, S.H. Kamarudin, M. Rayung, M.R.M. Asyraf, H.A. Aisyah, M.N.F. Norrrahim, R.A. Ilyas, N. Abdullah, E.S. Zainudin, S.M. Sapuan, A. Khalina, Mechanical Performance and Applications of CNTs Reinforced Polymer Composites — A Review, Nanomater. Rev. 11 (2021) 2186. https://doi.org/https://doi.org/10.3390/nano11092186.

[58] D. Banerjee, T. Nguyen, T.J. Chuang, Mechanical properties of single-walled carbon nanotube reinforced polymer composites with varied interphase's modulus and thickness: A finite element analysis study, Comput. Mater. Sci. 114 (2016) 209–218. https://doi.org/10.1016/j.commatsci.2015.12.026.

[59] B. Arash, H.S. Park, T. Rabczuk, Tensile fracture behavior of short carbon nanotube reinforced polymer composites: A coarse-grained model, Compos. Struct. 134 (2015) 981–988. https://doi.org/10.1016/j.compstruct.2015.09.001.

[60] R. Nandhakumar, K. Venkatesan, A process parameters review on selective laser melting-based additive manufacturing of single and multi-material: Microstructure, physical properties, tribological, and surface roughness, Elsevier Ltd, 2023. https://doi.org/10.1016/j.mtcomm.2023.105538.

[61] A. Alhendal, Enhanced thermomechanical properties of epoxy-multiwalled CNT nano-composites, RSC Adv. 14 (2024) 35360–35372. https://doi.org/10.1039/d4ra06831a.

[62] R.S. Lakes, Viscoelastic solids (1998), CRC press, 2017.

[63] S.C. Her, K.Y. Lin, Dynamic mechanical analysis of carbon nanotube-reinforced nanocomposites, J. Appl. Biomater. Funct. Mater. 15 (2017) S13–S18. https://doi.org/10.5301/jabfm.5000351.

[64] O.A. Serenko, V.I. Roldughin, A.A. Askadskii, E.S. Serkova, RSC Advances The e ff ect of size and concentration of nanoparticles on the glass transition temperature of polymer nanocomposites †, (2017) 50113–50120. https://doi.org/10.1039/c7ra08152a.

[65] S. Napolitano, D. Cangialosi, Interfacial Free Volume and Vitrification: Reduction in Tg in Proximity of an Adsorbing Interface Explained by the Free Volume Holes Diffusion Model, 46 (2013) 8051–8053. https://doi.org/https://doi.org/10.1021/ma401368p.

[66] R. Azhar, A. Khan, X. Chen, H. Qi, J. Huang, M. Luo, A novel shift in the glass transition temperature of polymer nanocomposites : a molecular dynamics simulation study †, (2021) 12216–12225. https://doi.org/10.1039/d1cp00321f.